Nano Research

Open Access

Research Article

# Shedding light on the effect of pore orientation on hydrogenation over carbon-supported single-atom catalysts

Yangyang Fan[1], Jianfei Dang[1], Miao Jin[1], Kaiwei Liu[2], Yajing Han[3], and Liqiang Wang[1]✉

[1] School of Material Science and Engineering, Zhengzhou University, Zhengzhou 450001, China
[2] Shanghai Space Propulsion Technology Research Institute, Shanghai 201108, China
[3] College of Advanced Interdisciplinary Science and Technology (CAIST), Henan University of Technology, Zhengzhou 450001, China

Cite this article: *Nano Research*, **2026**, *19*, 94908540. https://doi.org/10.26599/NR.2026.94908540

**ABSTRACT:** Rational control of pore orientation holds great potential to enhance mass transfer in carbon-supported single-atom catalysts (SACs), thereby increasing single-atom site utilization and catalytic performance; however, this strategy remains underexplored in catalytic hydrogenation reactions. In this paper, cobalt single-atom catalysts supported on oriented porous carbon (Co-SAC/OPC) and cobalt single-atom catalysts supported on non-oriented porous carbon (Co-SAC/NOPC) were synthesized using the hard-template method, and their performance in hydrogenation reactions was systematically investigated using 1-chloro-4-nitrobenzene (p-CNB) hydrogenation as a model reaction. Results from experiments (diffusion, substrate size-dependent conversion, and recycling) and finite-element analysis show that oriented pores facilitate p-CNB diffusion more effectively than non-oriented pores. This faster transfer enhances the accessibility and utilization of single-atom cobalt sites, resulting in significantly improved hydrogenation performance of Co-SAC/OPC. This work establishes a general strategy for enhancing the performance of carbon-supported single-atom catalysts in hydrogenation catalysis and related reactions.

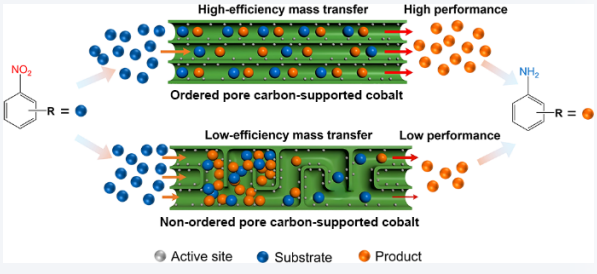


**KEYWORDS:** pore orientation, mass transfer, hydrogenation, site utilization, single-atom catalysts, metal (M)–N–C

## 1 Introduction

Nitrogen-doped carbon-supported metal (M, M = Fe, Co, and Ni) catalysts with atomically dispersed active sites (M–N–C) exhibit great potential to substitute noble metal-based catalysts for catalytic hydrogenation [1–5]. For example, our group found that N, S-coordinated cobalt single-atom catalysts (SACs) supported on hierarchically porous carbon (Co/NSC-AT) enable efficient hydrogenation of nitro compounds under mild conditions (35 °C, ~ 1 bar $H_2$) with high conversion (Con.) and selectivity (Sel.) [6]. In addition, Cao and co-workers demonstrated that $Co_1$/NPC SAC, featuring asymmetric $Co_1$–$N_3P_1$ sites, delivers exceptional activity and chemoselectivity for the hydrogenation of functionalized nitroarenes. In 1-chloro-4-nitrobenzene (p-CNB) hydrogenation, $Co_1$–$N_3P_1$ attains a turnover frequency (TOF) of 6560 $h^{-1}$, 60-fold higher than $Co_1$–$N_4$ [7]. Despite significant progress, SACs remain at an early stage, with their performance still falling short of industrial requirements, underscoring the need for performance-enhancing strategies.

Generally, the hydrogenation performance of M–N–C catalysts is governed by the intrinsic activity of single-atom sites (M–$N_x$) and their utilization [8–11]. Intrinsic activity—primarily dictated by the local coordination environment—has been extensively investigated [12–15]; by contrast, site utilization is increasingly recognized as equally critical. Unfortunately, many M–$N_x$ sites are confined within micropores or buried within carbon layers, limiting reactant accessibility and suppressing catalytic turnover [16–18]. Consequently, only a fraction of M–$N_x$ remains efficient under operating conditions, thereby reducing overall utilization. This limitation is especially pronounced in hydrogenation reactions: Substrates are often bulky and poorly soluble in the reaction medium [19–21]. Accordingly, efforts have focused on increasing site accessibility by improving reactant mass transfer, thereby enhancing active-site utilization.

Recent advances have highlighted the benefits of optimizing pore structure to enhance mass transfer, thereby improving site utilization [22–26]. For example, Shuai and co-workers reported that the concave Fe–N–C single-atom catalyst TPI@$Z_8$($SiO_2$)-650-C exhibits an enlarged external surface area and a high density of Fe–$N_4$ sites. The large external surface area and mesoporosity

**Received:** December 23, 2025; **Revised:** January 27, 2026
**Accepted:** February 4, 2026

✉Address correspondence to wangliqiang@zzu.edu.cn

increase site density by exposing previously inaccessible intraparticle Fe–$N_4$ sites, thereby improving mass transfer within the catalyst layer. Consequently, TPI@$Z_8$($SiO_2$)-650-C delivers high proton exchange membrane fuel cell (PEMFC) activity, achieving current densities of 0.022 A·cm$^{-2}$ at 0.9 $V_{iR\text{-free}}$ and 0.047 A·cm$^{-2}$ at 0.88 $V_{iR\text{-free}}$ under the U.S. Department of Energy (DOE) testing protocol [27]. Wang and co-workers prepared cobalt single atoms supported on a hollow-on-hollow carbon monolith ($Co_1$/HOHC-M) by pyrolyzing an α-cellulose monolith loaded with core–shell PS@Zn-zeolitic imidazolate framework (ZIF) nanospheres. The resulting structure features a large internal cavity (~ 290 nm) and a porous shell with hollow spherical pores (~ 10 nm). This hierarchical architecture enhances mass transfer and active-site accessibility, enabling high activity in the transfer hydrogenation of p-CNB to aniline. $Co_1$/HOHC-M achieves a reaction rate of 421.6 mmol·$g_{Co}^{-1}$·$h^{-1}$, surpassing the $Co_1$/HCS analog lacking hollow mesopores (353.8 mmol·$g_{Co}^{-1}$·$h^{-1}$) [28]. Although these strategies effectively increase single-atom site utilization, they continue to focus on optimizing pore size, pore volume, and surface area to enhance site accessibility and reaction efficiency.

On the other hand, mass transfer in porous catalysts is also highly dependent on pore orientation [29–32]. A non-oriented pore structure, especially one with misaligned and tortuous pore networks, hinders diffusion, whereas an oriented pore structure, such as straight, well-connected channels, facilitates mass transfer [33, 34]. Rationally, pore orientation could also influence site utilization and, ultimately, catalytic performance. Despite its importance, the impact of pore orientation on the catalytic performance of M–N–C, especially in catalytic hydrogenation, has received limited attention.

Herein, we assess how pore orientation influences the hydrogenation of p-CNB over cobalt single-atom catalysts supported on non-oriented porous carbon (Co-SAC/NOPC) and cobalt single-atom catalysts supported on oriented porous carbon (Co-SAC/OPC). The non-oriented catalyst (Co-SAC/NOPC) outperformed its oriented counterpart (Co-SAC/OPC) by roughly threefold in catalytic activity. Experiment and theoretical simulation reveal that this enhancement arises from faster p-CNB diffusion in the oriented pore network, which improves access to single-atom sites and increases their spatial and temporal utilization. In contrast, non-oriented channels are more susceptible to local blockage and mass-transfer limitations, limiting site utilization and overall activity.

## 2 Results and discussion

### 2.1 Preparation and characterization of Co-SAC/OPC and Co-SAC/NOPC

Co-SAC/OPC and Co-SAC/NOPC with different pore orientations were synthesized using the hard-template method, as previously reported with some modifications [19]. During synthesis, the hard template servesd as a structural guide and a confinement scaffold, directing precursor growth to replicate its structure and thereby enabling control over the pore structure of the catalyst [35]. Specifically, we first synthesized two silica molecular sieves, Santa Barbara amorphous-15 (SBA-15) and Mobil composition of matter-48 (MCM-48), as hard templates (Figs. S1(a) and S1(b) in the Electronic Supplementary Material (ESM)). Then, templates (SBA-15 or MCM-48) were dispersed in an aqueous solution of cobalt(II) chloride hexahydrate and o-phenylenediamine (oPD). Ammonium persulfate (APS) was then added to initiate oxidative polymerization of oPD, yielding Co-oPD/$SiO_2$ composites. After drying and pyrolysis, the materials underwent sequential NaOH/acid etching to remove silica and metallic nanoparticles (NPs), affording carbon-supported Co single atoms (Co-SACs). Since MCM-48 is a mesoporous silica with a three-dimensional bicontinuous channel network, the gained Co-SAC is expected to possess non-oriented pores (denoted as Co-SAC/OPC) [36]. By contrast, SBA-15 features an ordered two-dimensional hexagonal array of parallel cylindrical mesopores, yielding catalysts with oriented pores (denoted as Co-SAC/NOPC).

X-ray diffraction (XRD) patterns of the gained Co-SAC/OPC and Co-SAC/NOPC were displayed in Fig. S3 in the ESM; no peaks belonging to metallic Co were observed, suggesting that large Co nanoparticles were removed entirely after acid etching, and the remaining Co was well dispersed on the carbon matrices. Raman spectroscopy of Co-SAC/OPC and Co-SAC/NOPC reveals similar intensity ratios ($I_D/I_G$) of 0.99 and 0.98, respectively (Fig. S4 in the ESM). This indicates that both catalysts have comparable levels of graphitization and defect density. Transmission electron microscope (TEM) images of the two catalysts show no large particles in Co-SAC/OPC and Co-SAC/NOPC, consistent with the XRD results. To provide a deep insight into the dispersion of the Co element, aberration-corrected high-angle annular dark-field scanning TEM (AC-HAADF-STEM). The analysis was further performed. As shown in Fig. 1, bright dots were clearly observed and atomically dispersed on the carbon matrices (Figs. 1(b) and 1(e)). Although trace carbon-encapsulated nanoparticles persist after rigorous acid treatment, they are catalytically inert and have a negligible impact on the hydrogenation reaction (Fig. S4 in the ESM and Table 1). The Co content within Co-SAC/OPC and Co-SAC/NOPC was determined by inductively coupled plasma optical emission spectrometry (ICP-OES) to be 5.76 wt.% and 6.31 wt.%, respectively. As expected, Co-SAC/OPC and Co-SAC/NOPC have different pore orientations due to the directional growth of the templates. As shown in Figs. 1(a) and 1(d), Co-SAC/OPC possesses an oriented pore structure, and these well-defined pore structures arise from the structural features of the hard templates. In contrast, Co-SAC/NOPC has a non-oriented pore structure. $N_2$ adsorption and desorption experiments were further conducted to gain a deeper insight into the pore structure. As shown in Fig. 2(a), Co-SAC/OPC and Co-SAC/NOPC exhibit similar Type IV hysteresis loops, indicating that they possess a hierarchical pore structure. The pore size distribution further confirms this result, with pore sizes centered at 1 and 4 nm (Fig. 2(b)). Note that Co-SAC/OPC and Co-SAC/NOPC have similar pore volumes. Specifically, the pore volumes of Co-SAC/OPC for micropore and mesopore were 0.11 and 0.32 cm$^3$·g$^{-1}$, respectively, and those for Co-SAC/NOPC are 0.14 and 0.39 cm$^3$·g$^{-1}$ (Table S1 in the ESM), respectively. Overall, cobalt single-atom catalysts dispersed on nitrogen-doped carbon matrices with two distinct pore orientations have been successfully synthesized.

To better understand the electronic properties of Co in Co-SAC/OPC and Co-SAC/NOPC, we analyzed the oxidation states of Co and N by X-ray photoelectron spectroscopy (XPS). As shown in Figs. 3(a) and 3(c), the Co 2p XPS spectra can be resolved into three species: Co–$N_x$ (782.6 eV), $Co^{2+}$ (780.2 eV), and $Co^0$ (778.3 eV). Both catalysts exhibit comparable peak positions and similar Co-species proportions, indicating that Co atoms in both catalysts occupy a similar oxidation state (close to $Co^{2+}$) [37]. We also

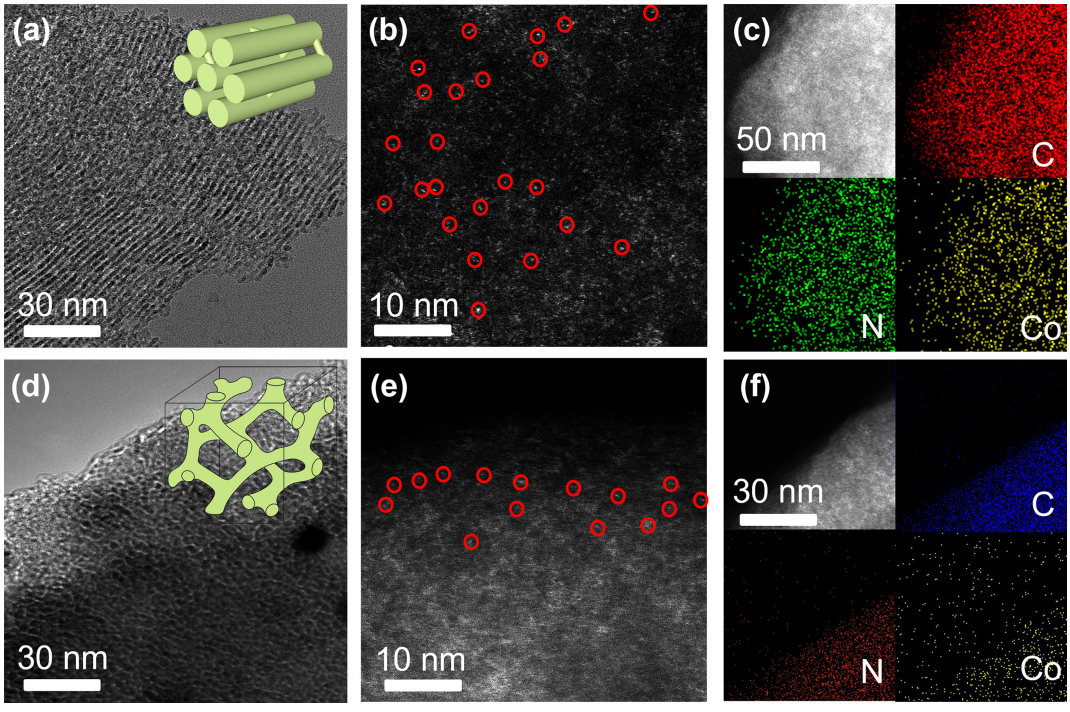


**Figure 1** Microscopic characterization of Co-SAC synthesized from different hard templates. ((a) and (d)) TEM images of Co-SAC/OPC and Co-SAC/NOPC. The insets are corresponding cartoon images of Co-SAC/OPC and Co-SAC/NOPC. ((b) and (e)) HAADF-STEM images of Co-SAC/OPC and Co-SAC/NOPC. ((c) and (f)) Energy dispersive X-ray spectroscopy (EDS) mapping images of Co-SAC/OPC and Co-SAC/NOPC.

**Table 1** Catalytic performances of different catalysts in the hydrogenation reaction of p-CNB[a]

| Entries | Catalysts | *P* (bar) | *T* (°C) | *t* (h) | Con. (%) | Sel. (%) |
|---|---|---|---|---|---|---|
| 1 | Co-SAC/OPC | 5 | 80 | 3 | 95 | > 99 |
| 2 | Co-SAC/NOPC | 5 | 80 | 3 | 75 | > 99 |
| 3 | Co-SAC/OPC[b] | 5 | 80 | 3 | 92 | > 99 |
| 4 | Co-SAC/NOPC[b] | 5 | 80 | 3 | 69 | > 99 |
| 6 | Co-SAC/OPC[c] | 5 | 120 | 3 | 100 | > 99 |
| 7 | Co-SAC/NOPC[c] | 5 | 120 | 3 | 79 | > 99 |
| 8 | C/OPC[d] | 5 | 80 | 3 | 0 | 0 |
| 9 | C/NOPC[d] | 5 | 80 | 3 | 0 | 0 |
| 10 | Co-SAC/OPC[e] | 5 | 80 | 3 | 58 | > 98 |
| 11 | Co-SAC/NOPC[e] | 5 | 80 | 3 | 57 | > 98 |

[a]Reaction conditions: catalyst, 10 mg; p-CNB, 30 mg; solvent, 10 mL (the volume ratio of ethanol (EtOH) to water ($V_{EtOH}/V_{H_2O}$) = 4:1). [b]Reaction conditions: not etched by $H_2SO_4$. [c]Reaction conditions: except that $H_2$ was substituted with 5 bar CO, other reaction conditions are the same as those in [a]. [d]The catalyst was prepared without the addition of cobalt salts. [e]The solvent is 100 mL ($V_{EtOH}/V_{H_2O}$ = 4:1) for the reaction; other conditions remain the same.

observed a strong peak at 778.2 eV in both catalysts, attributed to inert metallic Co. In Figs. 3(b) and 3(d), the N 1s XPS spectra of Co-SAC/OPC and Co-SAC/NOPC resolve four nitrogen species: pyridinic N (~ 398.5 eV), pyrrolic N (~ 399.8 eV), graphitic (quaternary) N (~ 400.9 eV), and oxidized N (~ 402.5 eV) [36, 38]. The total N content and relative proportion of these species are similar between Co-SAC/OPC and Co-SAC/NOPC. Collectively, XPS revealed similar surface compositions for Co-SAC/OPC and Co-SAC/NOPC: Co, 1.21 at.% vs. 1.29 at.%; N, 3.33 at.% vs. 3.42 at.%; and Co–$N_x$, 15.5 at.% vs. 16.1 at.%. Notably, both catalysts possess nearly identical Co–$N_x$ contents and electronic states.

The fine structures of Co-SAC/OPC and Co-SAC/NOPC were further analyzed by X-ray absorption near-edge structure (XANES) spectroscopy. In particular, the Co K edges of both samples are similar and lie between the Co metal and CoO edges (Fig. 3(e)). Extended X-ray absorption fine spectroscopy (EXAFS) further revealed the localized coordination nature of the cobalt atoms (Fig. 3(f)), with Co-SAC/OPC and Co-SAC/NOPC *k*-space at 2.0 Å (Table S3 in the ESM), which suggests that there is Co–N coordination in the first layer [6]. Weak signals from metallic Co were observed in Co-SAC/OPC and Co-SAC/NOPC, consistent with the XPS results. In addition, the EXAFS fitting results indicate that the central Co atom is coordinated to approximately 4 N atoms in Co-SAC/OPC and Co-SAC/NOPC (the coordination numbers of the central cobalt atoms in Co-SAC/OPC and Co-SAC/NOPC are determined to be approximately 4.24 and 4.36, respectively, as shown in Table S3 in the ESM). These results strongly suggest that Co-SAC/OPC and Co-SAC/NOPC have similar physical and chemical properties.

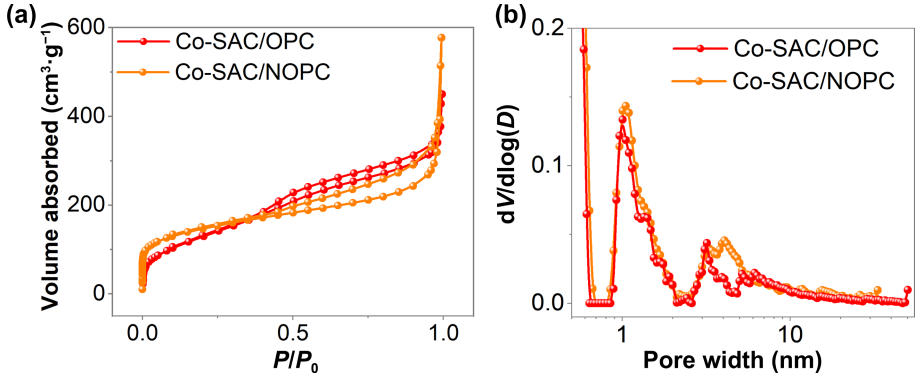


**Figure 2** (a) $N_2$ adsorption–desorption curves. (b) Pore size distribution of Co-SAC/OPC and Co-SAC/NOPC.

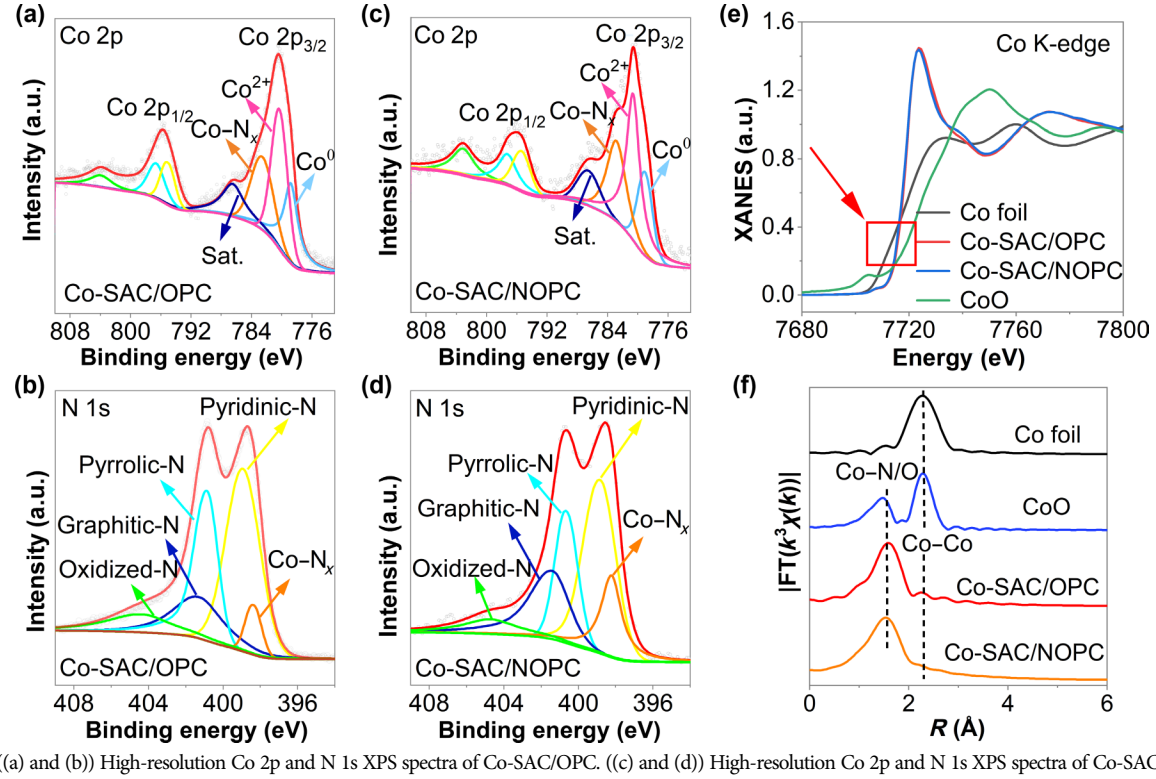


**Figure 3** ((a) and (b)) High-resolution Co 2p and N 1s XPS spectra of Co-SAC/OPC. ((c) and (d)) High-resolution Co 2p and N 1s XPS spectra of Co-SAC/NOPC. (e) XANES spectra of Co-SAC/OPC, Co-SAC/NOPC, CoO, and Co foil. (f) Fourier-transform EXAFS spectra of Co-SAC/OPC, Co-SAC/NOPC, CoO, and Co foil.

## 2.2 Hydrogenation performance of Co-SAC/OPC and Co-SAC/NOPC

Catalytic performance of Co-SAC/OPC and Co-SAC/NOPC was assessed using p-CNB hydrogenation as a model reaction. As summarized in Table 1 (Entries 1, 2, 8, and 9), the Co-free controls exhibited negligible activity. Upon cobalt incorporation, both Co-SAC/OPC and Co-SAC/NOPC catalysts became active, indicating that Co provides the primary active sites. Notably, Co-SAC/OPC outperformed Co-SAC/NOPC despite its lower Co loading (5.76 wt.%), smaller specific surface area, and reduced pore volume (Table S1 in the ESM). Note that both catalysts showed excellent resistance to CO poisoning (Table 1, Entries 6 and 7). Further analysis of the solvent effect revealed that the two catalysts performed significantly better in protonated solvents (water, methanol, ethanol) than in non-protonated solvents (cyclohexane, toluene, tetrahydrofuran) (Fig. S5 in the ESM). This is because proton solvents can promote the transfer of active hydrogen species from the catalyst surface to the substrate, thereby enhancing hydrogenation efficiency [39, 40]. The results above suggest that Co-SAC/OPC and Co-SAC/NOPC possess similar active sites.

To confirm that the active sites are the atomically dispersed Co, we conducted further analysis. Single-atom sites exhibit high acid resistance, whereas metal nanoparticles do not. We first tested the performance of both catalysts after acid etching and found that it showed almost no change (Table 1, Entries 3 and 4). Additionally, the ICP content of the catalysts did not change significantly after acid etching (Table S2 in the ESM). These results imply that the single-atom site is the leading active site for both catalysts. Generally, on single-atom sites, $H_2$ is typically activated via heterolytic cleavage, yielding a pronounced kinetic isotope effect (KIE) when $H_2$ is replaced by $D_2$ during p-CNB hydrogenation. As shown in Figs. S6 and S7 in the ESM, the reaction rate declined when $H_2$ (reaction rate constant with normal hydrogen ($k_H$)) was substituted by $D_2$ (reaction rate constant with deuterium ($k_D$)), attributable to the zero-point energy difference between the isotopic

isomers [16, 41]. Specifically, the $k_H/k_D$ for Co-SAC/OPC and Co-SAC/NOPC were 2.30 and 2.25, respectively, and are higher than those of the non-acid-etched catalysts (both are 1.97). The result suggests that $H_2$ is more likely to dissociate on Co–$N_x$ sites within Co-SAC/OPC and Co-SAC/NOPC via heterolytic cleavage, affording Co–H and N–H, with the latter possessing a significantly higher bond energy. Therefore, a more pronounced KIE could be observed for Co-SAC/OPC and Co-SAC/NOPC than in samples without acid etching when $H_2$ was substituted with $D_2$. The results suggest that Co–$N_x$ is the leading active site, and Co NPs made a limited contribution. A potassium thiocyanate (KSCN) poisoning experiment was also conducted to help distinguish the active sites (Fig. S8 in the ESM). Compared with carbon-encapsulated metallic Co, atomically dispersed Co is more likely to be poisoned by $SCN^-$ to some extent [16, 42]. As shown in Fig. S8 in the ESM, upon introduction of KSCN into the reaction system, aniline conversion decreased by 20%. These findings suggest that Co–$N_x$ sites play a crucial role in driving this reaction, whereas nanosized metallic Co contributed little to the catalytic activity of Co-SAC/OPC and Co-SAC/NOPC [43].

### 2.3 Mechanistic study of the relationship between pore orientation and catalytic performance

Of the many factors governing SAC performance, two are pivotal: intrinsic activity and single-atom-site utilization efficiency, the latter being primarily determined by mass transfer. To decouple intrinsic activity from utilization efficiency (i.e., diffusion effects), we diluted the reaction mixture to mitigate mass-transfer limitations (Table 1, Entries 10 and 11). Under these conditions, Co-SAC/OPC and Co-SAC/NOPC exhibited comparable hydrogenation rates, with TOFs of $7.33 \times 10^{-3}$ and $7.16 \times 10^{-3}$ $s^{-1}$, respectively. At high substrate-to-catalyst ratios and elevated substrate concentrations, Co-SAC/OPC outperforms Co-SAC/NOPC, with TOF values of $9.56 \times 10^{-1}$ and $1.36 \times 10^{-1}$ $s^{-1}$ (Table 1, Entries 1 and 2), respectively. Thus, the apparent advantage in activity at high concentration primarily reflects differences in site utilization governed by mass transfer.

Liquid-phase mass transfer proceeds in two steps: external diffusion from the bulk solution to the catalyst surface and internal diffusion within the pores. It is governed by factors, such as stirring speed, temperature ($T$), concentration, pressure ($P$), solvent properties, and the size and shape of the solute. Stirring primarily influences external diffusion, whereas temperature, concentration, and pressure mainly affect internal diffusion. To determine which mass-transfer mechanisms are more sensitive to pore orientation, we examined how these variables influence hydrogenation rates. Reaction rates for Co-SAC/OPC and Co-SAC/NOPC are negatively affected by stirring speed (Fig. S9 in the ESM) but diverge with changes in concentration (Fig. S10 in the ESM), pressure (Fig. S11 in the ESM), and temperature (Figs. 4(e) and 4(f) and Fig. S12 in the ESM). These results indicate negligible differences in external diffusion between the two catalysts; the observed performance gap arises mainly from differences in internal pore diffusion. Overall, oriented pores enhance mass transfer; by contrast, non-oriented pore networks create transient junction traps that generate concentration hotspots, hinder mass transfer, and diminish active-site utilization [44, 45].

To confirm these results, we performed liquid-phase adsorption–desorption measurements of p-CNB on Co-SAC/OPC and Co-SAC/NOPC. Adsorption and desorption experiments are the direct means of demonstrating mass transfer phenomena, the core of which lies in inferring the substance transfer process by observing the dynamics of adsorbed substances at the interface and inside the adsorbent [46, 47]. Specifically, p-CNB was incubated with Co-SAC/OPC or Co-SAC/NOPC under stirring; time-dependent p-CNB solution concentrations were quantified by ultraviolet–visible (UV–vis) spectrophotometry. As shown in Fig. 4(c), during the first 15 min, when external diffusion predominates, UV–vis absorbance decreased similarly in both systems, indicating no discernible difference in this regime. Beyond 15 min, generally regarded as the internal periods, Co-SAC/OPC showed a more pronounced absorbance decline than Co-SAC/NOPC, indicating faster internal diffusion in the oriented-pore material and a more rapid transfer of p-CNB from the catalyst surface into the pore network. Furthermore, desorption was monitored by stirring p-CNB-loaded Co-SAC/OPC and Co-SAC/NOPC in water and quantifying the time-dependent p-CNB concentration by UV–vis spectrophotometry (Fig. 4(d)). Throughout the experiment, the Co-SAC/OPC system consistently exhibited higher solution concentrations than the Co-SAC/NOPC system, indicating faster desorption. Notably, Co-SAC/OPC reached a substantially higher equilibrium solution concentration, indicating partial intraparticle retention of p-CNB within Co-SAC/NOPC. To exclude substrate-specific effects, p-CNB was substituted with methylene blue. Under these conditions, Co-SAC/OPC and Co-SAC/NOPC continued to exhibit similar adsorption–desorption behaviors (Fig. S14 in the ESM). These results suggest that the oriented pore structure of Co-SAC/OPC facilitates internal diffusion of p-CNB. In contrast, the non-oriented pores of Co-SAC/NOPC impose greater internal mass-transfer resistance.

Considering the above, it is speculated that pore orientation significantly influences substrate mass transfer, which, in turn, governs the utilization of single-atom sites and, consequently, catalytic performance (Fig. 4(a)). To validate this mechanism, we quantified size-dependent conversion across different catalysts and assessed their recycling stability, two metrics governed by mass transfer. On the one hand, we performed hydrogenation reactions on a substrate library spanning kinetic diameters ($d_k$) [48] and plotted conversion versus $d_k$ (Table S4 in the ESM). For Co-SAC/OPC, substrates with $d_k < 7.3$ Å, where p-CNB has $d_k = 7.3$ Å, exhibit only a gradual decline in conversion; when $d_k > 7.3$ Å (Fig. 4(b)), pore-channel confinement dominates and conversion drops sharply. Despite comparable pore sizes, Co-SAC/NOPC shows a more distinctive performance decline, even for small molecules, than Co-SAC/OPC during the recycling periods. Such a result indicates that non-oriented, tortuous channels promote molecular retention and intensify diffusion limitations. On the other hand, mass-transfer limitations also accelerate catalyst deactivation by accumulating reactants, intermediates, and products that block active sites within the porous structure. To test the influence of orientation in this situation, we conducted recycling experiments. After ten cycles, both catalysts exhibited declining activity. Note that the activity can be fully restored through thermal treatment (Figs. S13 and S14 in the ESM), indicating that deactivation is reversible and primarily caused by the embedding of active sites rather than permanent site loss [49]. This conclusion is corroborated by TEM, ICP-OES, and scanning electron microscopy (SEM) results, which show that structural integrity is maintained throughout the deactivation–regeneration cycle (Figs. S20 and S21 and Table S2 in the ESM). In detail, Co-SAC/NOPC declined sharply within the first three cycles, whereas Co-SAC/OPC only

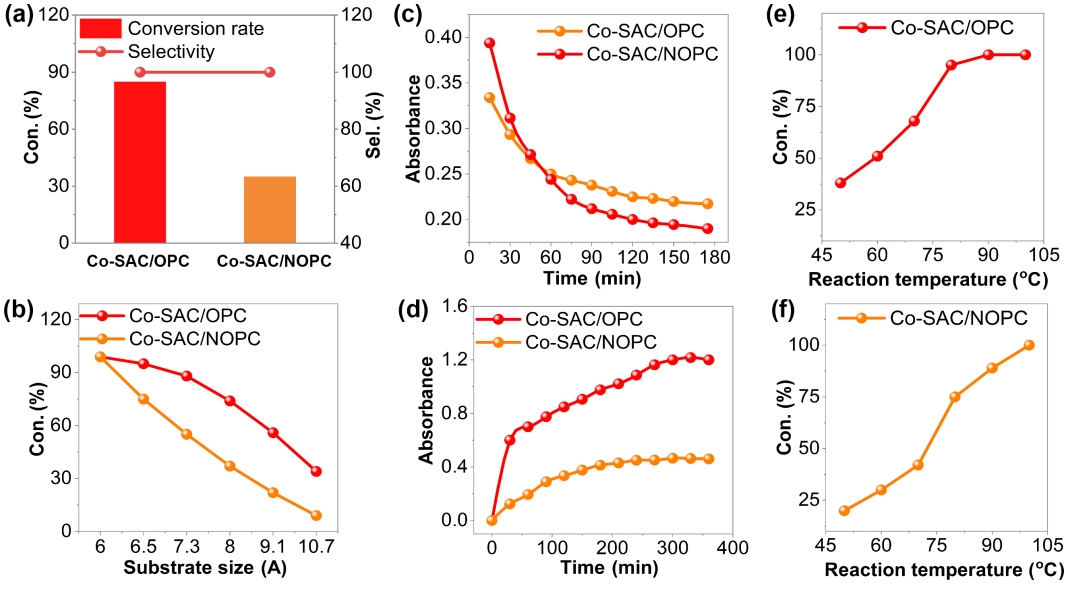


**Figure 4** Mechanism investigation experiments. (a) Comparison of the performance of the two catalysts for 1 h of reaction. (b) Sensitivity testing of Co-SAC/OPC and Co-SAC/NOPC to substrate size. Test conditions: 10 mg catalyst, 0.25 mmol substrate, 80 °C, 3 h. (c) Comparative testing of Co-SAC/OPC and Co-SAC/NOPC adsorption for p-CNB. (d) Comparative testing of Co-SAC/OPC and Co-SAC/NOPC desorption for p-CNB. ((e) and (f)) Co-SAC/OPC and Co-SAC/NOPC sensitivity tests to temperature.

underwent a gradual decline under identical conditions. The catalyst regeneration experiment indicates that the activity of the deactivated Co-SAC/OPC can be restored at a lower temperature than that of Co-SAC/NOPC (Figs. S15 and S16 in the ESM), indicating that pore deposits are more readily removed in Co-SAC/OPC. Collectively, these results suggest that oriented pore architectures enhance mass transfer, improve single-atom-site utilization, and thereby increase catalytic performance.

To further elucidate the mass-transfer property of p-CNB within Co-SAC/OPC and Co-SAC/NOPC, we performed finite-element simulations with time-resolved particle tracking to evaluate the influence of pore architecture on transport. To differentiate the effect of pore orientation on mass transfer, we simplified the models based on prior studies: a one-directional transport model (Model/OPC) to represent Co-SAC/OPC, and a three-directional transport model (Model/NOPC) to represent Co-SAC/NOPC (Fig. S17 in the ESM). A particle with a molecular volume comparable to p-CNB was utilized as a tracer. The mass transfer properties of Model/OPC and Model/NOPC were elucidated using COMSOL by recording the time-dependent spatial distribution of particles, the transport rate, and the time required for the particles to reach dynamic equilibrium. As shown in Fig. 5, at time ($t$) = 0.000 s, no particles entered either model. For $t \geq 0.003$ s, both models exhibit substantial particle influx, and the particles increase over time. Model/OPC exhibits an approximately uniform particle distribution along the diffusion axis. By contrast, Model/NOPC shows accumulation at the initial diffusion boundary (left side) and progressive congestion along the axis. Over time, congestion intensifies, evidenced by increased particle accumulation near the boundary and a reduced effective diffusion rate due to frequent interparticle collisions. This jamming substantially impedes transport, producing a pronounced left–right asymmetry in particle density. Notably, at $t$ = 0.01 s, Model/OPC has reached diffusive equilibrium, whereas Model/NOPC has not (Fig. S18 in the ESM). The above results indicate that pore orientation significantly influences mass transfer, and a catalyst with an optimized orientation can greatly improve mass transfer efficiency and active site utilization, thereby enhancing catalyst performance.

## 3 Conclusions

In summary, we systematically investigated how pore orientation in carbon-supported single-atom catalysts affects their hydrogenation performance. Co-SAC/OPC and Co-SAC/NOPC were designed and synthesized for the catalytic hydrogenation of p-CNB. Experiments show that, compared with non-oriented pores, oriented pores are more likely to accelerate reactant diffusion and product desorption, thereby increasing the spatiotemporal utilization of Co–$N_x$ sites. As a result, the activity of Co-SAC/OPC is nearly three times higher than that of Co-SAC/NOPC. Finite element simulations performed with COMSOL software also confirmed the higher mass transfer efficiency of the Model/OPC model with oriented pores. Specifically, particle diffusion within the Model/OPC exhibited no discernible blockage, whereas particle diffusion within the Model/OPC encountered severe blockage, with this obstruction progressively worsening over time. These findings establish pore orientation—along with pore size and surface area—as a key structural parameter that dictates active-site utilization and catalytic performance, thereby providing a mechanistic basis and design principles for developing efficient and durable carbon-supported SACs for hydrogenation and related reactions.

**Electronic Supplementary Material**: Supplementary material (additional experiment details and data, SEM images, TEM images, pore size distribution curves, XRD patterns, and $N_2$ adsorption–desorption isotherms of samples) is available in the online version of this article at https://doi.org/10.26599/NR.2026.94908540.

## Data availability

All data needed to support the conclusions in the paper are presented in the manuscript and the Electronic Supplementary Material. Additional data related to this paper may be requested from the corresponding author upon request.

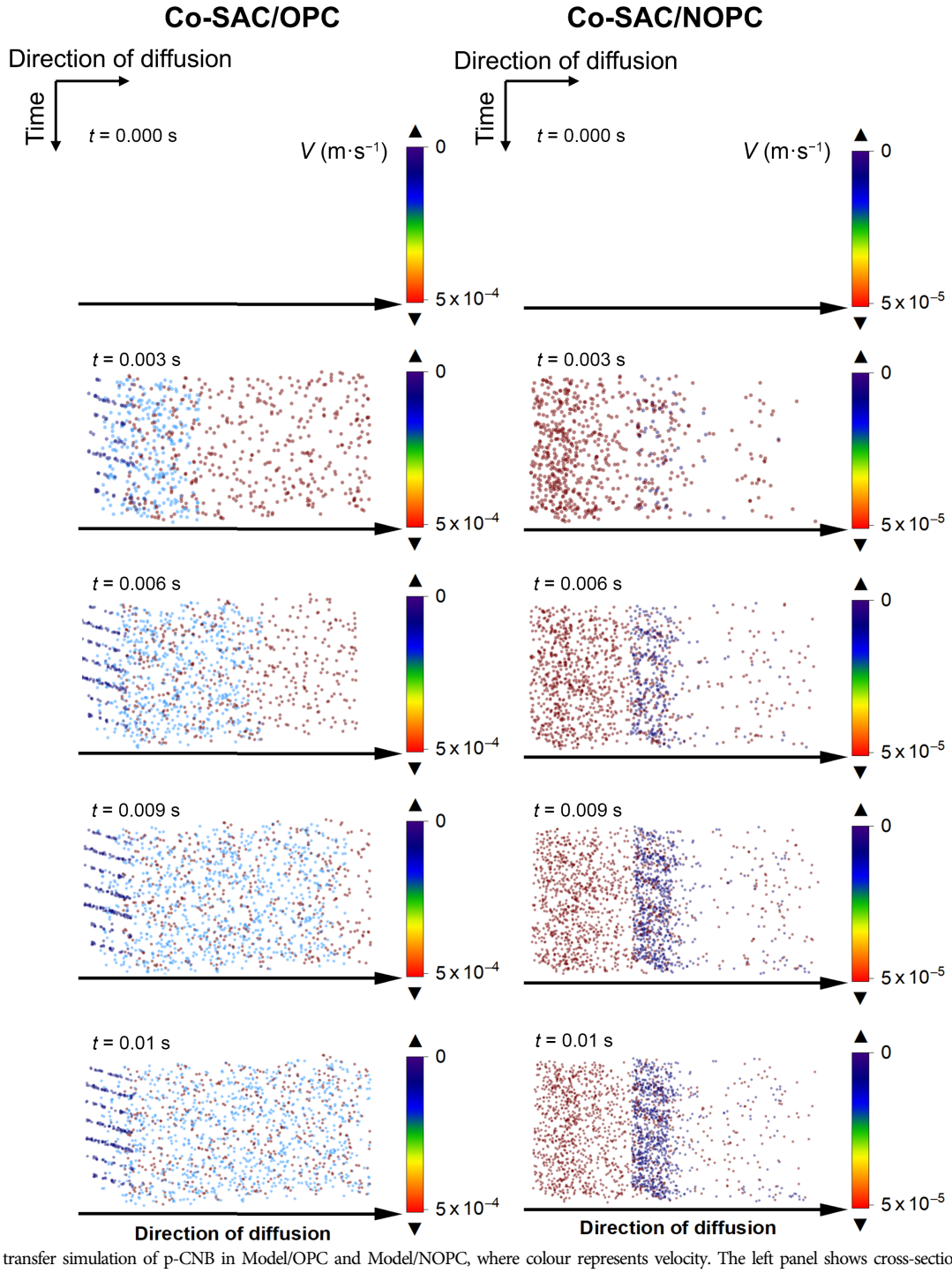


**Figure 5** Mass transfer simulation of p-CNB in Model/OPC and Model/NOPC, where colour represents velocity. The left panel shows cross-sectional views of the physical positions of Model/OPC at $t$ = 0.000, 0.003, 0.006, 0.009, and 0.01 s. The right panel shows cross-sectional views of the physical positions of Model/NOPC at $t$ = 0.000, 0.003, 0.006, 0.009, and 0.01 s.

## Acknowledgements

This work was supported by the National Natural Science Foundation of China (Nos. 22478363, 22238013, 22008221, and 22404043), the Excellent Young Scientists Fund of Henan Province (No. 252300421177), the Key Scientific Research Projects of Colleges and Universities in Henan Province (No. 25A530001), the Postdoctoral Fellowship Program of China Postdoctoral Science Foudation (CPSF, No. GZC20240417), and the Start-up Grant of Henan University of Technology (No. 2023BS023).

## Declaration of competing interest

All the contributing authors report no conflict of interests in this work.

## Author contribution statement

Y. Y. F.: Data curation, project administration, validation, writing manuscript, and experimental design. J. F. D.: Data curation, project administration, writing manuscript, and experimental

design. M. J.: Writing manuscript. K. W. L.: Project administration, funding acquisition. Y. J. H.: writing manuscript. L. Q. W.: Project administration, funding acquisition, writing manuscript. All the authors have approved the final manuscript.

## Use of AI statement

None.

## References


[1] Li, J. J.; Jiang, Y. F.; Wang, Q.; Xu, C. Q.; Wu, D. J.; Banis, M. N.; Adair, K. R.; Doyle-Davis, K.; Meira, D. M.; Finfrock, Y. Z. et al. A general strategy for preparing pyrrolic-$N_4$ type single-atom catalysts via pre-located isolated atoms. *Nat. Commun.* **2021**, *12*, 6806.

[2] Mehmood, A.; Gong, M. J.; Jaouen, F.; Roy, A.; Zitolo, A.; Khan, A.; Sougrati, M. T.; Primbs, M.; Bonastre, A. M.; Fongalland, D. et al. High loading of single atomic iron sites in Fe–NC oxygen reduction catalysts for proton exchange membrane fuel cells. *Nat. Catal.* **2022**, *5*, 311–323.

[3] Hai, X.; Xi, S. B.; Mitchell, S.; Harrath, K.; Xu, H. M.; Akl, D. F.; Kong, D. B.; Li, J.; Li, Z. J.; Sun, T. et al. Scalable two-step annealing method for preparing ultra-high-density single-atom catalyst libraries. *Nat. Nanotechnol.* **2022**, *17*, 174–181.

[4] Gao, D. W.; Zhang, X.; Dai, X. P.; Qin, Y. C.; Duan, A. J.; Yu, Y. B.; Zhuo, H. Y.; Zhao, H. R.; Zhang, P. F.; Jiang, Y. et al. Morphology-selective synthesis of active and durable gold catalysts with high catalytic performance in the reduction of 4-nitrophenol. *Nano Res.* **2016**, *9*, 3099–3115.

[5] Cui, X. K.; Liu, K. W.; Han, Y. J.; Wang, L. Q. Rational design of single-atom catalysts for efficient hydrogenation of nitro compounds. *Chem. Synth.* **2025**, *5*, 79.

[6] Wang, C. Q.; Dang, J. F.; Han, Y. J.; Zeng, Q. G.; Wang, L. Q. Carbon nanotube-supported Co–N–C with enriched mesopores for hydrogenation of nitro compounds. *J. Catal.* **2025**, *447*, 116152.

[7] Jin, H. Q.; Li, P. P.; Cui, P. X.; Shi, J. A.; Zhou, W.; Yu, X. H.; Song, W. G.; Cao, C. Y. Unprecedentedly high activity and selectivity for hydrogenation of nitroarenes with single atomic $Co_1$–$N_3P_1$ sites. *Nat. Commun.* **2022**, *13*, 723.

[8] Wu, Z. Y.; Zhu, P.; Cullen, D. A.; Hu, Y. F.; Yan, Q. Q.; Shen, S. C.; Chen, F. Y.; Yu, H. R.; Shakouri, M.; Arregui-Mena, J. D. et al. A general synthesis of single atom catalysts with controllable atomic and mesoporous structures. *Nat. Synth.* **2022**, *1*, 658–667.

[9] Lin, M. J.; Hao, C.; Yang, B.; Liu, J.; Tan, C. F.; Wang, Z. H.; Xie, Y. L.; Shen, P. K.; Tian, Z. Q. Ultra-low Pt loading cathode catalyst layers with hierarchically mesoporous distribution modulation for high-performance proton exchange membrane fuel cells. *Nano Res.* **2025**, *18*, 94907824.

[10] Ren, Z. X.; Lian, L. Z.; Zuo, X. L.; Cui, X. K.; Zhang, M.; Deng, L.; Wang, L. Q.; Liu, Y. N. Electronically modulated defective $Cu_{1.81}S$ by $FeN_4$ for high-performance nitroarene hydrogenation. *Adv. Funct. Mater.*, in press, DOI: 10.1002/adfm.202524811.

[11] Guan, J. P.; Huang, C. Y.; Liu, D. H.; Li, B.; Wang, T. H.; Gong, J. X.; Liu, X.; Zheng, H. R.; Xiong, Y. Fe single atom-doped on canola meal-derived carbon for efficient oxygen reduction reaction. *Nano Res.* **2026**, *19*, 94908051.

[12] Zhang, G. J.; Tang, F. Y.; Wang, X.; Wang, L. Q.; Liu, Y. N. Atomically dispersed Co–S–N active sites anchored on hierarchically porous carbon for efficient catalytic hydrogenation of nitro compounds. *ACS Catal.* **2022**, *12*, 5786–5794.

[13] Zhao, X. J.; Wang, J.; Lian, L. Z.; Zhang, G. J.; An, P.; Zeng, K.; He, H. C.; Yuan, T. C.; Huang, J. H.; Wang, L. Q. et al. Oxygen vacancy-reinforced water-assisted proton hopping for enhanced catalytic hydrogenation. *ACS Catal.* **2023**, *13*, 2326–2334.

[14] Zhang, Y.; Li, Y.; Cheong, W. C.; Liu, S. J.; Zhuang, Z. W.; Chen, C. One-pot synthesis of single-atom iridium on ordered mesoporous carbon-based materials for direct dehydrogenation of lower alkanes. *Nano Res.* **2026**, *19*, 94907867.

[15] Lou, Y. Z.; Wei, J. Q.; Li, M. F.; Zhu, Y. Distal ionic substrate-catalyst interactions enable long-range stereocontrol: Access to remote Quaternary stereocenters through a desymmetrizing Suzuki–Miyaura reaction. *J. Am. Chem. Soc.* **2022**, *144*, 123–129.

[16] Zhao, X. J.; Wang, L. Q.; Zhang, G. J.; An, P.; Yu, M.; Lian, L. Z.; Zhang, C. C.; Ouyang, D. C.; Yan, Y. C.; Chen, L. M. et al. Breaking the trade-off between CO tolerance and intrinsic activity in hydrogenation on metal oxide-supported noble metal single atoms through coordination environment engineering. *ACS Catal.* **2024**, *14*, 15325–15335.

[17] Yu, M.; Zhang, G. J.; Li, K.; Tang, F. Y.; Wang, L. Q.; Liu, Y. N. Ni nanoparticles decorated Ni–N–C catalyst: Dual-site synergy for enhanced catalytic hydrogenation. *AIChE J.* **2025**, *71*, e18830.

[18] Ren, W. C.; Yang, L.; Wang, X. Y.; Qiu, C. L.; Shi, J.; Chen, J. W.; Tian, W. Q.; Huang, M. H.; Wang, H. L. Synergistic $CO_2$ etching and carbonization induces closed-pore structures for plateau-dominant sodium storage. *Nano Res.* **2025**, *18*, 94908108.

[19] Perovic, M.; Tarakina, N. V.; Hofmann, J. P.; Oschatz, M. Influence of local environments in pores of different size on the catalytic liquid-phase oxidation of D-glucose by au nanoparticles supported on nanoporous carbon. *ACS Appl. Nano Mater.* **2020**, *3*, 7695–7703.

[20] Nawaz, M. A.; Blay-Roger, R.; Saif, M.; Meng, F. H.; Bobadilla, L. F.; Reina, T. R.; Odriozola, J. A. Redefining the symphony of light aromatic synthesis beyond fossil fuels: A journey navigating through a Fe-based/HZSM-5 Tandem route for syngas conversion. *ACS Catal.* **2024**, *14*, 15150–15196.

[21] Lou, F. J.; Zhang, G. H.; Ren, L. M.; Guo, X. W.; Song, C. S. Impacts of nano-scale pore structure and organic amine assembly in porous silica on the kinetics of $CO_2$ adsorptive separation. *Nano Res.* **2021**, *14*, 3294–3302.

[22] Zhang, Q.; Wang, S.; Jiang, N.; Jiang, B. L.; Liu, Y. X.; Chen, Y. G.; Li, F.; Song, H. Design of a highly active $TiO_2$-supported $Ni_2P$@C catalyst with special flower-like radial channels for quick p-cresol hydrodeoxygenation. *J. Catal.* **2024**, *432*, 115338.

[23] Zheng, Y. K.; Wang, Q. L.; Yang, C.; Qiu, T. Experimental study on mass transport mechanism in poly (styrene-co-divinylbenzene) microspheres with hierarchical pore structure. *Chem. Eng. Process. Process Intensif.* **2019**, *139*, 183–192.

[24] Shi, Y. J.; Zhou, Y. W.; Lou, Y.; Chen, Z. P.; Xiong, H. F.; Zhu, Y. F. Homogeneity of supported single-atom active sites boosting the selective catalytic transformations. *Adv. Sci.* **2022**, *9*, 2201520.

[25] Zhang, C. C.; Chabu, J. M.; Wang, L. Q.; Liu, Y. N. Construction of Ni–$O_V$–Ti sites through strong metal–support interactions for selective hydrogenation of nitroarenes to anilines. *Chem. Eng. J.* **2025**, *521*, 166785.

[26] Bai, S. X.; Yan, P. X.; Li, B. B.; Zhu, X. F.; He, L.; Kuang, M.; Yang, J. P. Mechanisms and challenges of nanoporous confinement for carbon dioxide electrocatalysis. *Nano Res.* **2026**, *19*, 94907935.

[27] Wan, X.; Liu, X. F.; Li, Y. C.; Yu, R. H.; Zheng, L. R.; Yan, W. S.; Wang, H.; Xu, M.; Shui, J. L. Fe–N–C electrocatalyst with dense active sites and efficient mass transport for high-performance proton exchange membrane fuel cells. *Nat. Catal.* **2019**, *2*, 259–268.

[28] Gong, X. Y.; Li, D. C.; Zhang, Q.; Wang, W. Q.; Tian, Z. B.; Su, G.; Huang, M. H.; Wang, G. H. Cobalt single atoms supported on monolithic carbon with a hollow-on-hollow architecture for efficient transfer hydrogenations. *Nano Res.* **2023**, *16*, 11358–11365.

[29] Khandekar, D. C.; Bhattacharyya, A. R.; Bandyopadhyaya, R. Role of axial versus radial pore orientation in mesoporous silica particles, on its effect in photocatalysis via impregnated $TiO_2$ nanoparticles in pores. *Chem. Eng. J. Adv.* **2021**, *5*, 100075.

[30] Li, Y. Y.; Shen, H. Y.; Zhu, Y. Y.; Zada, I.; Song, F.; Liu, Q. L.; Pan, H.; Zhu, S. M.; Li, J.; Kasal, B. et al. Hierarchical pore engineering of lignocellulose-based carbon materials for electric double-layer capacitors. *Nano Res.* **2025**, *18*, 94907960.

[31] Wang, L. Q.; Xiong, H. L.; Zheng, Y. N.; Yang, J. Q.; Wang, Y.; Qiao, Z. A. A polymer derived bubble templates strategy towards perovskite oxides with tunable pore structure and rich surface-active sites for boosting aerobic oxidation of benzyl alcohol. *Nano Res.* **2025**, *18*, 94907653.

[32] Jia, Z. Y.; Tang, B. T.; Wang, W. T.; Zhang, S. F.; Zhang, Y. A. Ternary synergistic structure of Co–TiN@CNTs enables efficient electromagnetic wave absorption through coupling of multi-loss mechanisms. *Nano Res*., in press, DOI: 10.26599/nr.2026.94908414.

[33] Huang, X.; Zhou, W.; Liu, B.; Jiang, K. Y. Pore network modeling of advection-diffusion-reaction in porous media: The effects of channels. *Chem. Eng. Sci.* **2023**, *271*, 118577.

[34] Feng, J. T.; Wang, F.; Han, X. X.; Ao, Z.; Sun, Q. M.; Hua, W. D.; Chen, P. P.; Jing, T. W.; Li, H. Y.; Han, D. A "green pathway" different from simple diffusion in soft matter: Fast molecular transport within micro/nanoscale multiphase porous systems. *Nano Res.* **2014**, *7*, 434–442.

[35] Huang, Y. H.; Gu, J.; Hu, Y. D.; Lei, Y. J.; Yu, T.; Wang, C. Preparation of mesoporous carbon with adjustable diameter and pore size. *Diamond Relat. Mater.* **2022**, *130*, 109515.

[36] Chen, Z. L.; Wu, R. B.; Liu, Y.; Ha, Y.; Guo, Y. H.; Sun, D. L.; Liu, M.; Fang, F. Ultrafine Co nanoparticles encapsulated in carbon-nanotubes-grafted graphene sheets as advanced electrocatalysts for the hydrogen evolution reaction. *Adv. Mater.* **2018**, *30*, 1802011.

[37] Yang, L.; Cao, X. J.; Wang, X. J.; Wang, Q. L.; Jiao, L. F. Regulative electronic redistribution of $CoTe_2$/CoP heterointerfaces for accelerating water splitting. *Appl. Catal. B: Environ.* **2023**, *329*, 122551.

[38] Xiong, W.; Zhou, S. S.; Wang, L. P.; Liu, Y.; Hao, F.; Liu, P. L.; Luo, H. A. ZIF-derived Co-based catalysts for efficient hydrogenation of aromatic compounds: The study of the Co–$N_x$ active sites. *Ind. Eng. Chem. Res.* **2020**, *59*, 22473–22484.

[39] Gloag, L.; Somerville, S. V.; Gooding, J. J.; Tilley, R. D. Co-catalytic metal-support interactions in single-atom electrocatalysts. *Nat. Rev. Mater.* **2024**, *9*, 173–189.

[40] Guo, J. F.; Chin, Y. H. C. Rationalizing Solvent effect in bronsted acid-catalyzed C–O scission: A thermodynamically consistent framework with assessable descriptors. *ACS Catal.* **2025**, *15*, 19040–19056.

[41] Lu, M. L.; Liu, Y. S.; Yang, F.; Ge, Y. X.; Shi, X. D.; Mao, Y. Q.; Song, X. Y.; Li, Z. J.; Li, J. J.; Lyu, Y. X. et al. $Ga_2O_3$-modified Cu–ZnO catalysts for efficient hydrogen production from aqueous-phase reforming of methanol. *ACS Catal.* **2025**, *15*, 18782–18793.

[42] Li, X.; Qi, G. D.; Lewis, R. J.; Howard, M. J.; Murrer, B. A.; Harrison, B.; Morgan, D. J.; Kiely, C. J.; He, Q.; Davies, T. E. et al. Partial oxidation of methane to acetic acid with oxygen using AuPd/ZSM-5. *ACS Catal.* **2025**, *15*, 18663–18674.

[43] Xie, T. Q.; Peng, Q.; Cao, G. M.; Wu, Z. W.; Xie, L. L.; Ma, S. G.; Shi, H.; Jiang, X. Oxygen vacancy-rich $TiO_2$-supported single-atom Ru catalysts for stable and selective demethoxylation of lignin-derived phenolic monomers. *ACS Catal.* **2025**, *15*, 18438–18449.

[44] Jadav, D.; Shukla, P.; Bandyopadhyay, R.; Kubota, Y.; Das, S.; Bandyopadhyay, M. Tetranuclear Zn complex covalently immobilized on sulfopropylsilylated mesoporous silica: An efficient catalyst for ring opening reaction of epoxide with amine. *Mol. Catal.* **2020**, *497*, 111220.

[45] Jaramillo, L. Y.; Henao, W.; Romero-Sáez, M. Synthesis and characterization of MCM-41-SBA-15 mixed-phase silica with trimodal mesoporous system and thick pore wall. *J. Porous Mater.* **2020**, *27*, 1669–1676.

[46] Inglezakis, V. J.; Balsamo, M.; Montagnaro, F. Liquid–solid mass transfer in adsorption systems—An overlooked resistance. *Ind. Eng. Chem. Res.* **2020**, *59*, 22007–22016.

[47] Zhang, W.; Vilensky, R.; Zussman, E.; Yarin, A. L. Adsorption and mass transfer in granular porous membranes/media due to inserted volatile materials. *Int. J. Heat Mass Transf.* **2018**, *116*, 248–258.

[48] Soto, C.; Torres-Cuevas, E. S.; Palacio, L.; Prádanos, P.; Freeman, B. D.; Lozano, Á. E.; Hernández, A.; Comesaña-Gándara, B. Gas permeability, fractional free volume and molecular kinetic diameters: The effect of thermal rearrangement on *ortho*-hydroxy polyamide membranes loaded with a porous polymer network. *Membranes* **2022**, *12*, 200.

[49] Chen, R. Z.; Wang, X. Y.; Dang, J. F.; Yun, S. J.; Wang, L. Q.; Kong, F. G.; Liu, Y. N. Shedding light on the reversible deactivation of carbon-supported single-atom catalysts in hydrogenation reaction. *Nano Res.* **2024**, *17*, 4807–4814.